

PROCEEDINGS A

rspa.royalsocietypublishing.org



Article submitted to journal

Subject Areas:

fluid mechanics, material science, volcanology

Keywords:

three phase, bubble suspension, rheology, analogue experiments, lava flows

Author for correspondence:

J. Birnbaum

e-mail: janineb@ldeo.columbia.edu

THE ROYAL SOCIETY
PUBLISHING

Rheology of three-phase suspensions determined via dam-break experiments

J. Birnbaum¹, E. Lev¹ and E. W. Llewellyn²

¹Lamont-Doherty Earth Observatory, Columbia University, 61 Rte. 9w, Palisades, NY, 10964, US

²Department of Earth Sciences, Durham University, Durham DH1 3LE, UK

Three-phase suspensions, of liquid that suspends dispersed solid particles and gas bubbles, are common in both natural and industrial settings. Their rheology is poorly constrained, particularly for high total suspended fractions ($\gtrsim 0.5$). We use a dam-break consistometer to characterize the rheology of suspensions of (Newtonian) corn syrup, plastic particles, and CO₂ bubbles. The study is motivated by a desire to understand the rheology of magma and lava. Our experiments are scaled to the volcanic system: they are conducted in the non-Brownian, non-inertial regime; bubble capillary number is varied across unity; and bubble and particle fractions are $0 \leq \phi_{gas} \leq 0.82$ and $0 \leq \phi_{solid} \leq 0.37$ respectively. We measure flow-front velocity and invert for a Herschel–Bulkley rheology model as a function of ϕ_{gas} , ϕ_{solid} , and the capillary number. We find a stronger increase in relative viscosity with increasing ϕ_{gas} in the low to intermediate capillary number regime than predicted by existing theory, and find both shear-thinning and shear-thickening effects, depending on the capillary number. We apply our model to the existing community code for lava flow emplacement, PyFLOWGO, and predict increased viscosity and decreased velocity compared with current rheological models, suggesting existing models may not adequately account for the role of bubbles in stiffening lavas.

1. Introduction

Two-phase liquid–solid (particle) and liquid–gas (bubble) suspensions are important across nature and industry. Consequently, their behavior has been well characterized: see Mader et al. [1] for a through review. Numerous stu-

© The Authors. Published by the Royal Society under the terms of the Creative Commons Attribution License <http://creativecommons.org/licenses/by/4.0/>, which permits unrestricted use, provided the original author and source are credited.

dies show that the apparent viscosity of particle suspensions increases with particle volume fraction, and intermediate and concentrated suspensions show non-Newtonian behavior with finite yield stresses and strain-rate dependence [2, 3, 4]. Bubble suspensions exhibit an increase or decrease in apparent viscosity relative to the liquid phase. Concentrated bubble suspensions also show non-Newtonian behavior, including non-zero yield stresses and shear-thinning or shear-thickening behavior [5, 6, 7, 8, 9, 10, 11, 12, 13, 14, 15]. A key parameter determining the rheology of bubble suspensions is the capillary number:

$$\text{Ca} = \frac{\mu a \dot{\gamma}}{\Gamma}, \quad (1.1)$$

where μ is the liquid viscosity, a is the undeformed bubble radius, $\dot{\gamma}$ is the shear strain rate, and Γ is the surface tension. The capillary number reflects the ratio of viscous stresses that deform bubbles and capillary stresses that restore them [7, 13, 14]. When $\text{Ca} \gg 1$, viscous stress dominates, bubbles deform easily and decrease relative viscosity; when $\text{Ca} \ll 1$, the surface tension resisting bubble deformation dominates, bubbles remain nearly spherical and increase relative viscosity.

The rheology of three-phase suspensions (liquid suspending particles and bubbles) has received much less detailed investigation, but is known to be a complex function of the suspended phase fractions, micro-textural properties such as the size and shape distributions of particles and bubbles, and the conditions of shear [10, 16, 17]. The only systematic experimental study, which was limited to $\phi_{\text{solid}} \lesssim 0.5$, $\phi_{\text{gas}} \lesssim 0.3$ and low capillary number [17], found that the rheology was well described by a simple convolution of existing two-phase rheology models in which the liquid and bubbles were treated as an effective medium that suspended the particles. We expect that interactions between bubbles and particles will become increasingly important at higher bubble and particle fractions such that a simple convolution of two-phase models is insufficient.

Magma (and lava, which is its subaerial counterpart) is a natural three-phase suspension, composed of a molten silicate liquid (melt) that suspends a variable fraction of solid particles (crystals) and gas bubbles. The suspending melt is Newtonian over a wide range of strain rates, and has a viscosity that can vary over orders of magnitude [18, 19]. Bubble and crystal volume fractions can both range from 0 to 1, and typically change, along with melt viscosity, during transport through the Earth's crust and over its surface. The rheology of magma exerts a first-order control on the dynamics of its eruption, and the emplacement of subsequent lava flows [20, 21]. Whilst the rheology of natural magmas has been measured directly [22, 23, 24, 25], such measurements are challenging to perform and interpret, and are not well suited to systematic investigation of parameter space. As a result, it has been common for rheology of magmatic suspensions to be investigated via analogue experiments [4, 6, 13, 17, 26]. Even with the use of analogues, it has proven challenging to perform rheometry on samples with $\phi_{\text{gas}} \gtrsim 0.5$. This is because samples with high bubble fraction are difficult to prepare, particularly when the sample also contains particles, and because they are prone to breakdown when loaded into a conventional rheometer. We conduct experiments in which bubbles are grown *in situ* via a chemical reaction, and analysed using a dam-break consistometer. This approach circumvents both problems, allowing us to investigate samples with bubble fractions ($0 \leq \phi_{\text{gas}} \leq 0.8$) and particle fractions ($0 \leq \phi_{\text{solid}} \leq 0.37$) that span the most relevant ranges for natural magma and lava.

2. Theoretical background

(a) Scaling

We scale our analogue suspensions to basaltic magma, which typically has a pure-melt viscosity in the range 10^2 to 10^4 Pas (10^3 – 10^5 Poise) at eruption temperature [19], and surface tension between 0.05 and 0.3 N/m [27, 28, 29]. Bubbles that nucleate deep within the volcanic plumbing system are likely to be small (radius $\sim 10^{-5}$ to 10^{-3} m) and experience very low shear rates

($\sim 10^{-10}$ to 10^{-5} 1/s), resulting in capillary numbers $Ca \ll 1$ [30, 31]. As magmas decompress on their way to the surface, bubbles grow and coalesce to radii $\sim 10^{-5}$ – 10^{-2} m or larger [32, 33, 34]. However, decimeter sized bubbles often segregate from the flow, making a suspension rheology approach no longer appropriate. Magma in basaltic dikes experiences strain rates up to $\sim 10^1$ to 10^2 1/s [35] and capillary number therefore spans from $Ca \ll 1$ to $Ca \gg 1$. At the surface, lava flows, particularly fast-moving flows (velocities ~ 1 m/s) may experience strain rates of 10^{-3} to 10^2 1/s, and both high and low capillary numbers [8]. The viscosity of silicate melts is sufficiently high that viscous stresses at the particle scale dominate over inertial and Brownian stresses [4]. We therefore conduct experiments that span from low to high capillary number, whilst remaining in the non-inertial, non-Brownian regimes.

(b) Theoretical framework for rheology of three-phase suspensions

To our knowledge, the only theoretically-grounded model for the rheology of three-phase suspensions is that of Phan-Thien and Pham [16]. They present a model for the effective Newtonian viscosity, η , of a three-phase suspension of the form:

$$\eta_{r,s} = \frac{\eta}{\mu} = \eta_{r,p} \eta_{r,b} \quad (2.1)$$

where $\eta_{r,s}$ is the relative viscosity of the three-phase suspension (i.e. suspension viscosity normalized by the liquid viscosity), and $\eta_{r,p}$ and $\eta_{r,b}$ are the relative viscosities of the two-phase components (particle-liquid, and bubble-liquid suspensions respectively). Importantly, this relation treats one two-phase system as an effective viscous medium in which the third phase is suspended. Truby et al. [17] validated this theoretical form against experimental data, using existing models for the viscosity of the two-phases suspensions:

$$\eta_{r,p} = \left(1 - \frac{\phi_{solid}}{\phi_m}\right)^{-B_{solid}}, \quad \text{and} \quad \eta_{r,b} = (1 - \phi_{gas})^{-B_{gas}}, \quad (2.2)$$

following, respectively, Mueller et al. [4] and Llewellyn and Manga [7], where Einstein exponents $B_{solid} = 2$ and $B_{gas} = 1$, and ϕ_m is a maximum packing fraction of solid particles. Both Phan-Thien and Pham [16] and Truby et al. [17] note that the definition of ϕ_{gas} and ϕ_{solid} depends on which two-phase suspension is chosen as the effective medium; in this study we choose the particle suspension such that $\phi_{solid} = V_{solid}/(V_{solid} + V_{liquid})$ and $\phi_{gas} = V_{gas}/(V_{gas} + V_{solid} + V_{liquid})$, where V denotes the volume of the subscript phase.

Truby et al. [17] extend the model of Phan-Thien and Pham [16] to allow for non-Newtonian effects by equating the suspension viscosity, η , with the consistency, K , in the Herschel-Bulkley model [36]:

$$\tau = \tau_y + K \dot{\gamma}^n, \quad (2.3)$$

where τ is the shear stress, τ_y is the yield stress, and n is the flow index ($n > 1$ implies shear-thickening, $n < 1$ shear-thinning). We adopt this approach in the analysis below.

3. Methods

(a) Experimental setup

Our experiments use a Bostwick (dam-break) consistometer, in which fluid is released from a reservoir and into a confined rectangular channel (Fig. 1). The reservoir measures 20 cm along the length of the channel, and the channel extends another 1 m; the reservoir and channel have a constant width of 15 cm. The reservoir can be filled to a maximum depth of 15 cm, and in our experiments initial reservoir depth ranges from 4 to 13 cm. The walls of the consistometer are transparent to allow observation and imaging of the flow. We use 42DE corn syrup diluted to a 77% sugar concentration, measured using a Brix refractometer. Corn syrup is a Newtonian fluid with a viscosity that depends on water-content (dilution) and temperature. Our experiments are

conducted at room temperature (isothermal for a given experiment) which varied between 18.1 and 30.5 °C, corresponding to syrup viscosities in the range $13.3 \leq \mu \leq 3.73$ Pa s, measured using a Brookfield rotational viscometer. The surface tension of corn syrup is $\Gamma = 0.08$ N/m [37]; the surface tension of sugar solutions is only weakly dependent on concentration [38].

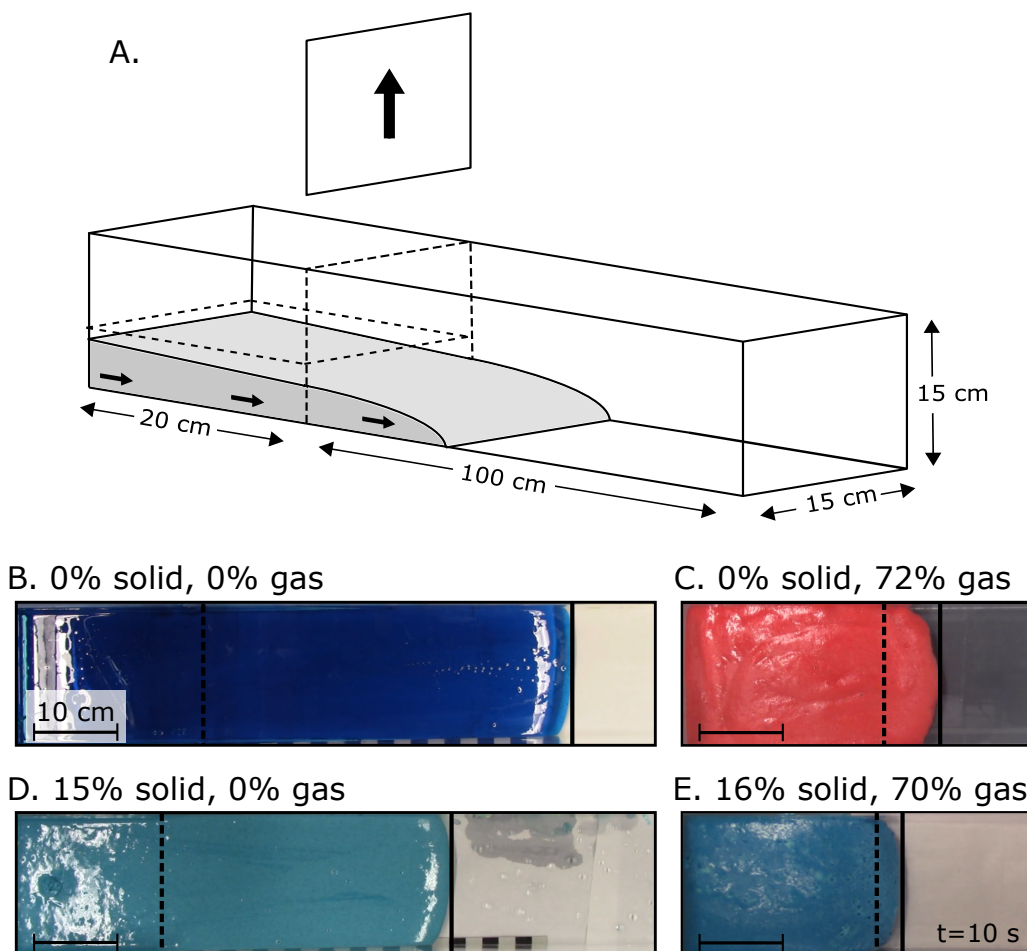


Figure 1. A) Dam-break setup showing fluid release into a confined channel. B-E) Top views contrasting the slower flow-front progression with the addition of particles and bubbles, with starting position (dashed) and position 10 s after dam removal (solid). All photos have the same scale.

To the syrup, we add rigid plastic particles sieved to a mesh size of 60-80 (Sourced from Precise Finishing Inc Stock No. GP-PP60/80, Polyplus / Type II). Particles have near-neutral buoyancy ($\rho_{syrup} = 1395$ kg/m³, $\rho_{plastic} = 1370$ kg/m³), are angular and slightly elongate (aspect ratio 1.5 to 2), and have a dominantly unimodal size distribution (long axis ≈ 200 to 400 μ m). Particles are stirred into the suspension by hand which leads to minimal air entrapment as shown in the microphotograph in Supplementary Fig. S2. Volume fraction of solids in the suspension is determined prior to the introduction of gas by mass of syrup and particles (uncertainty of 1-2 volume %). When multiple experiments with the same particle content were performed, a large volume of syrup and particles was prepared, but gas was introduced to each sample individually.

Gas is introduced via a chemical reaction between baking soda (NaHCO_3) and citric acid ($\text{C}_6\text{H}_8\text{O}_7$) which produces water vapor and CO_2 gas. Reactants are added with a $\sim 3:4$ ratio by mass, yielding an empirical relation of roughly 0.5 g baking soda and 0.7 g citric acid per 100 g syrup, per 10% desired gas volume fraction. The reaction begins immediately and the sample is allowed to rise for ~ 20 min prior to its release into the confined channel. Samples with $\phi_{gas} < 0.6$ are risen in a separate container, then transferred to the consistometer reservoir; samples with $\phi_{gas} > 0.6$ are more delicate, and are risen in the reservoir to avoid foam disruption during transfer. Final gas volume fraction is calculated from the final mixture density. Mass of the suspension is measured when transferring to the channel and the volume is calculated using the internal channel dimensions and the height of the mixture within the reservoir as measured through the channel walls. This method leads to ~ 3 to 5% relative uncertainty on the volume and resultant ~ 3 to 5% relative uncertainty on the density and an absolute uncertainty of ~ 0.02 to 0.04 on ϕ_{gas} .

The water vapor that forms during the reaction is insufficient to lower the syrup viscosity appreciably. In the experiments with the highest concentration of reactants (9 g total per 100 g of syrup), that water could, in principle, result in a dilution from 77% to 76.6% sugar if all the water dissolved, which would change the viscosity from 7.6 Pas (76 Poise) to 6.5 Pas (65 Poise) at 23°C . However, a test suspension, from which the evolved gas was allowed to escape overnight showed no additional dissolved water when analysed using the Brix refractometer.

The flow begins with the removal of the dam, which takes less than one second. The dam is typically coated with ~ 2 to 3 mm of syrup, when removed, effectively shortening the length of the fluid in the reservoir. However, in this geometry, propagation is insensitive to the length of the reservoir and this is below the spatial resolution of our forward model. Flow progression along the channel is recorded by time-lapse photographs from the side at a rate of 1 frame-per-second (FPS), and from above using a video camera (30 FPS). Experiments last between 15 and 180 s, with most 30 to 90 s in duration. We process the top-view videos to extract the flow front position over time. In the tracking algorithm, the video, rotated to align the flow direction left to right, is processed by manually identifying the starting position, scale, and center line in each video, and setting an appropriate threshold on the brightness of either the red, blue or green channel of the image to distinguish syrup from the background. In some cases, the time–distance profile of the flow front was smoothed to remove artifacts caused by the flash from the side-view camera. The flow front position is compared to a forward model of dam-break flow to invert for the rheological parameters.

(b) Extracting rheological parameters from experiments

We follow the derivations of Liu and Mei [39] and Balmforth et al. [40] for time evolution of flow thickness, h , of a Herschel–Bulkley fluid flowing down a slope:

$$\frac{\partial h}{\partial t} = \frac{\partial}{\partial x} \left[\left(\frac{\rho g}{K} \right)^{1/n} \frac{n \left| \sin \theta - \frac{\partial h}{\partial x} \cos \theta \right|^{1/n-1} Y^{1/n+1}}{(n+1)(2n+1)} \left((2n+1)h - nY \right) \left(\sin \theta - \frac{\partial h}{\partial x} \cos \theta \right) \right], \quad (3.1a)$$

$$Y = h - \frac{\tau_y}{\rho g \left| \sin \theta - \frac{\partial h}{\partial x} \cos \theta \right|}, \quad (3.1b)$$

where x is the along-channel distance, ρ is the fluid density, g is the acceleration due to gravity, and θ is the channel slope.

This forward model is valid for non-inertial laminar flow of a gravitationally settling fluid experiencing no-slip conditions at the base of the flow and no-stress at the free surface. In the inertial regime, propagation of the flow front would be expected to scale with the shallow water speed \sqrt{gH} . Based on the short-time similarity solution of the flow front position given by Balmforth et al. [40] for a Newtonian fluid, $X \sim 0.2845 \hat{t}^{1/2}$, for $t = \frac{L}{H} \left(\frac{KL}{\rho g H^2} \right)^{1/n} \hat{t}$ and $x = L\hat{x}$,

where L is the reservoir length and H the reservoir depth, we expect inertia would be dominant for $t \lesssim 10^{-5} - 10^{-2}$ s, which is much shorter than the duration of our experiments. We confirm that all experiments are in the laminar regime by verifying that the Reynolds number, Re , is below the cutoff for the onset of turbulence at $Re \sim 1000$. We calculate Re for a free surface flow of a Herschel-Bulkley fluid in a rectangular channel as $Re = \frac{\rho \bar{u}^{2-n} D^n}{(\tau_y/8)(D/\bar{u})^n + K((3m+1)/(4m))^n 8^{n-1}}$, $m = \frac{nK(8\bar{u}/D)^n}{\tau_y + K(8\bar{u}/D)^n}$ [41] where \bar{u} is the mean velocity, D is the hydrodynamic radius, $D = \frac{4HW}{2H+W}$, for channel width $W = 15$ cm, and channel depth $H \sim h$. We find Reynolds numbers $\lesssim 10$, well below the cutoff. We confirm no-slip conditions via imaging through the base of the channel, which shows that bubbles are well coupled to the base (Supplementary Fig. S3). We neglect the effect of surface tension between the syrup and air, which becomes important for $h < 2\sqrt{\frac{\Gamma}{\rho g}} \approx 0.5$ cm [42]. Accordingly, we restrict our experiments to have a starting reservoir volume $H > 4$ cm. Finally, we require that the suspension be able to deform under its own weight, which requires that the Bingham number, $B < 1$, where $B \equiv \frac{\tau_y L}{\rho g H^2}$ [40]. We prepared a suspension of $\phi_{solid} = 0.46$, and find that for a flow height of 2.5 cm, it does not deform under its own weight, suggesting that yield stress must exceed 42 Pa.

We solve equation 3.1a numerically using a finite-difference scheme on a centered 3-point stencil which is second-order accurate in space and we use two-step Runge-Kutte for second order accuracy in time. Initial conditions are fluid height $h = H$ where $x \leq L$ (within the reservoir), and $h = 0$ elsewhere. Boundary conditions are no-slip on the bottom, no-stress at the free surface, $\frac{\partial h}{\partial x}|_{x=x_L} = 0$ (no inflow on low slope), and $h|_{x=x_R} = 0$ where x_R is chosen to be sufficiently far from the final position of the flow front such that flow does not reach the far boundary (domain length is 20% longer than the final experimental flow length). The domain is discretized in space evenly with 52 grid points and with a constant time step of $\Delta t = 6.67 \times 10^{-4}$ s. The forward model assumes that temperature, rheology, and density fluid of the fluid are constant in time and space. We allow slope to be non-zero in the model solution to account for sensitivity of flow advance rate to slope angles below our uncertainty for direct measurement ($\leq 0.5^\circ$). We extract the position of the flow front over time from the model by identifying where $h \approx 0$, below a threshold of 1×10^{-4} to account for numerical diffusion, smoothed linearly between grid points in x .

We use the evolution of the flow front over time in the experiments as a constraining observation in our inversion for rheological parameters. We invert for rheological parameters (K, τ_y, n) and the slope (θ) using an Ensemble Kalman Filter (EnKF) approach [43, 44]. This is a probabilistic approach in which the forward model is instantiated many times with varying parameters that are modified iteratively to minimize the misfit between the model and data (typically ~ 2000 data points). All samples are propagated together between iterations, which allows faster convergence than a random walk. We use Gaussian priors centered about a visually-determined close fit for the rheological parameters, and about zero for the slope. Standard deviations were 10%, 10%, 5%, and 1° for the initial distributions of K, τ_y, n , and θ , respectively. EnKF simulations are initialized with 300 samples and run for 5 iterations; convergence is typically achieved within 4 iterations, insensitive to small changes in the initial parameters (Supplementary Fig. S5). In other Earth-science applications, EnKF is often used to update probabilities by assimilating more information through time, for example in volcano monitoring [43, 44]. We do not utilize this capability of EnKF; all information about the flow progression is included from the beginning. We use the Python implementation of the EnKF algorithm provided on GitHub by geoyanzhan3¹ [43, 44]. We report the numerically-determined maximum likelihood value, and uncertainty given by the 5% and 95% quantiles. We find uncertainty values of $\lesssim 20\%$ in K , $\lesssim 20\%$ in τ_y , and $\lesssim 10\%$ in n .

¹See https://github.com/geoyanzhan3/EnKF_tutorial

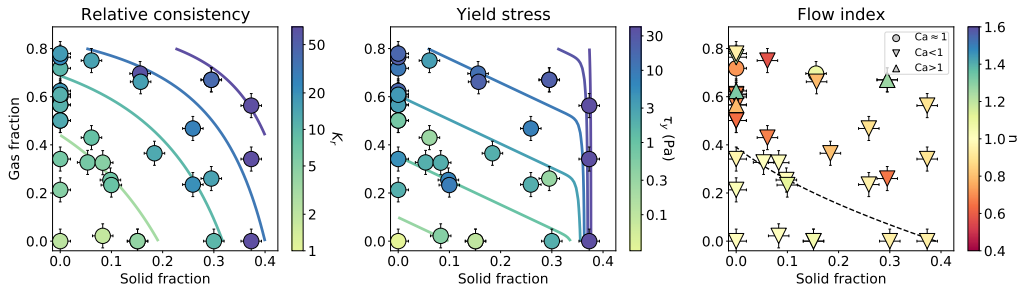


Figure 2. Experimental rheology measurements plotted against solid (x -axis) and gas (y -axis) volume fractions, and the value of A) relative consistency, K_r , and B) yield stress, τ_y shown in color. Contours represent the best-fitting empirical models on the same color scale. In panel C), color represents the maximum capillary number, Ca , and flow index, n , indicated by marker shape. The dashed black line indicates the critical volume fraction for the onset of shear-rate dependent behavior below which flow is shear-rate-independent, and above which shear-thinning behavior is expected at intermediate and low Ca and shear-thickening behavior is predicted for high Ca . Data are reported in Table S2.

4. Results

We present results from 35 dam-break experiments spanning $0 \leq \phi_{solid} \leq 0.37$ and $0 \leq \phi_{gas} \leq 0.82$ (Fig. 2 and Table S2). We find that, with increasing volume fraction of solids, relative consistency ($K_r = K/\mu$) increases, yield stress increases, and flow index decreases (more shear-thinning), consistent with previous studies [1]. Increasing gas fraction in all cases increases relative consistency and yield stress. Gas-bearing experiments show both shear-thinning ($n < 1$) and shear-thickening ($n > 1$) behavior, with increasing n correlated with increasing Ca .

We use our measurements to parameterize the model framework presented in Section 2b, and find empirical expressions for K_r , τ_y , and n as functions of phase volume fractions and (where relevant) the maximum capillary number. We calculate maximum capillary number using equation 1.1 with the maximum observed bubble size from each experiment (0.5 to 8.2 mm) and estimate the maximum strain rate from experiment videos. Best fitting parameter values for these empirical models are determined using the L-BFGS-B algorithm for limited-memory, quasi-Newton, bound-constrained optimization [45] implemented in Python; uncertainty is estimated from the approximated Hessian matrix.

We find the following empirical relationships:

$$K_r = \left(1 - \frac{\phi_{solid}}{\phi_m}\right)^{-B_{solid}} (1 - \phi_{gas})^{-B_{gas}}, \quad (4.1a)$$

$$\tau_y = 10^{C_1(\phi_{solid} - \phi_{c,\tau_y})} + 10^{C_2(\phi_{solid} + \phi_{gas} - \phi_{c,\tau_y})}, \quad (4.1b)$$

$$n = \begin{cases} 1, & \phi_{solid}(1 - \phi_{gas}) + \phi_{gas} \leq \phi_{c,n} \\ 1 + (C_3 - C_4 Ca)(\phi_{c,n} - \phi_{solid}(1 - \phi_{gas}) - \phi_{gas}), & \phi_{solid}(1 - \phi_{gas}) + \phi_{gas} > \phi_{c,n} \end{cases} \quad (4.1c)$$

where $\phi_m = 0.56 \pm 0.20$, $B_{solid} = 2.74 \pm 1.56$ and $B_{gas} = 1.98 \pm 0.09$, $C_1 = 80.0 \pm 10.9$, $C_2 = 1.98 \pm 0.23$, the critical volume fraction for the onset of appreciable yield stress $\phi_{c,\tau_y} = 0.35 \pm 0.01$, $C_3 = 0.70 \pm 0.25$, $C_4 = 0.55 \pm 0.31$, and the critical volume fraction for the onset of shear rate dependence $\phi_{c,n} = 0.39 \pm 0.12$. Results from each experiment are plotted in Fig. 2 and compared to contours for the best-fitting model plotted on the same color scale. Misfit between the experiments and model are given in Table S2.

5. Discussion

(a) Comparison with previous studies

(i) Relative Consistency, K_r

Our expression for consistency (Eq. 4.1a) has the functional form presented in Eq. 2.1, such that it can be decomposed into separate functions for the two-phase components, facilitating comparison with previous studies (Fig. 3A and 3D, equations and parameters in Table S4). For particle suspensions ($\phi_{gas} = 0$), we find a $K_r(\phi_{solid})$ dependence that has the same functional form as that of Krieger and Dougherty [3] and Roscoe [46]. We do not have experiments for $\phi_{solid} > 0.37$ where relative consistency rapidly increases and a transition to another functional form, such as that in Costa et al. [47], may be appropriate. For bubble suspensions ($\phi_{solid} = 0$) we find a $K_r(\phi_{gas})$ dependence that is stronger than most previous studies, with bubbles having a stronger stiffening effect on the suspensions. Furthermore, we find that in our experiments, bubbles always increase the relative consistency, regardless of capillary number, in contrast with previous studies [6, 13].

We note that our consistency model (Eq. 4.1a) is optimized against the full three-phase dataset, hence three-phase interactions are likely to play a role in these discrepancies with models that are fitted against two-phase data. For instance, breakup of bubbles between interacting particles, and the formation of liquid-film bridges between particles may both amplify the effect of the bubble fraction on suspension rheology, and cause the rheology to be controlled by the smallest bubbles, which are in the low Ca regime, despite observations of deformation in the largest bubbles (Fig. S2), which imply $Ca \gg 1$ locally.

(ii) Yield Stress, τ_y

We select an empirical exponential-type relationship for yield stress (Eq. 4.1b), which overlaps with previous two-phase studies (Fig. 3B and 3E). We observe a much stronger effect of particles compared to gas, but onset at around the same volume fraction. Yield stresses we observe in three-phase suspensions are higher than would be predicted by a linear superposition of the two-phase components, indicating again that interactions among the phases are important. At intermediate volume fractions we find moderately good agreement with Hoover et al. [49] and Mueller et al. [4]. The gas-liquid suspension experiments compare favorably to results by Princen and Kiss [11] and Rouyer et al. [12], although there is limited overlap between regions of calibration.

(iii) Flow Index, n

We fit flow index data using a piecewise continuous linear relationship after Castruccio et al. [26] and Truby et al. [17]. For particle suspensions, and for bubble suspensions at low Ca, this formulation yields a shear-thinning behavior, which is consistent with previous relationships (Fig. 3C and 3F). With increasing Ca and gas fraction, it transitions to shear-thickening, a behavior reported in previous studies [10].

(b) Data limitations

We use the dam-break consistometer setup to measure the rheology of three-phase suspensions in order to avoid bubble breakdown which is common in conventional rheometers. This setup allows us to attain high bubble volume fractions, but requires numerical inversion and additional considerations for direct comparison to rheometry data collected via other methods. The behavior of Herschel-Bulkley fluids in confined channels and on unconfined slopes has been investigated theoretically and experimentally [50], primarily using kaolin clay suspensions and Carbopol which show variable agreement with measurements collected in conventional rheometers. Most studies that use channel flow to investigate rheology use the approach to a final runout state [51], the height profile [52, 53, 54], the internal velocity [55, 56, 57, 58], or the runout distance with time

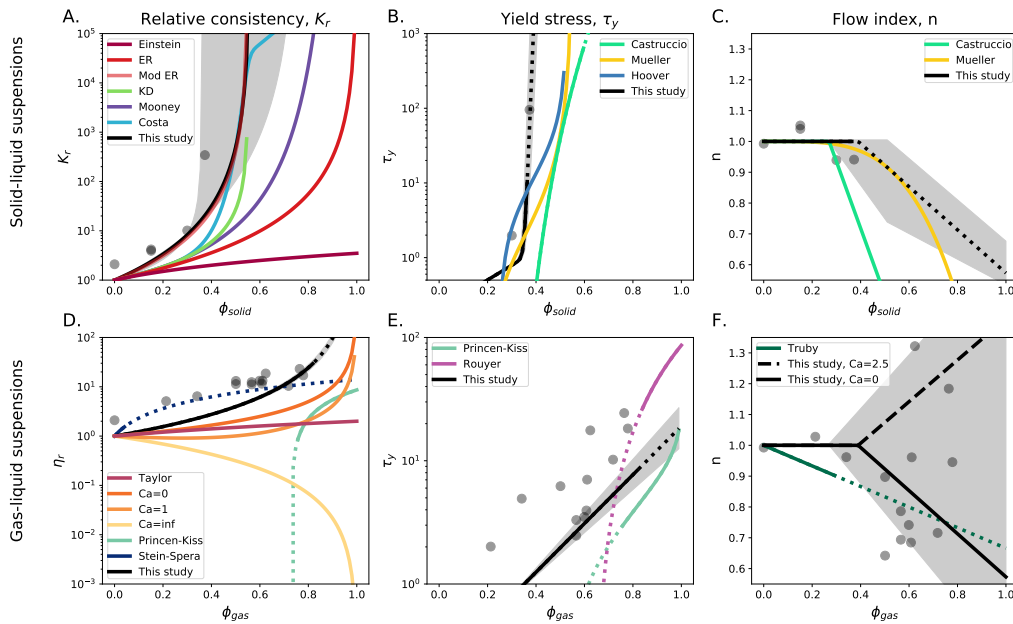


Figure 3. Comparison between popular rheology models and the model proposed in this study. A and D) show relative consistency, B and E) yield stress, and C and F) flow index in the two-phase end-member cases of A-C) solid-liquid only and D-F) gas-liquid only suspensions. Best-fit models for our experiments are plotted in black, with grey shaded regions highlighting model uncertainties. ER = Roscoe [46], KD = Krieger and Dougherty [3], Also see Mueller et al. [4], Llewellyn and Manga [7], Princen and Kiss [11], Rouyer et al. [12], Stein and Spera [14], Taylor [15], Truby et al. [17], Castruccio et al. [26], Costa et al. [47], Mooney [48], Hoover et al. [49] (See Table S4). Dotted lines indicate extrapolations outside the calibration region for experimental studies. Grey markers are our two-phase experiments. Note that the model is constrained on the three-phase dataset so does not necessarily pass through this subset of the experiments.

[40, 52, 59, 60]. The internal velocity and height profiles observed in experiments using kaolin clay typically compare favorably to theory, except during the initial slumping stage, in which inertia is dominant, and near the flow front where significant curvature requires more sophisticated modeling [53, 58]. In contrast, experiments using Carbopol show systematic offsets compared to conventional rheometers, possibly a result of basal slip, three-dimensional effects such as levee formation [55, 56], or a scale effect introduced in the narrow gap of conventional rheometers compared to a relatively large microstructural length scale in Carbopol [58]. Our results use the runout distance with time to measure rheology which shows good agreement with conventional rheometry for experiments on corn syrup, xanthan gum, and kaolin suspensions [40]. We expect our suspensions to behave similarly to two-phase kaolin particle suspensions, and further verify that basal slip and levee formation do not occur in our experiments. Given findings in previous work on two-phase suspensions in dam-break experiments and the good agreement between our experiments and existing particle-bearing suspensions, we do not expect systematic offsets in the rheometric parameters determined in our study compared to what would be measured in a conventional rheometer.

Our forward model is 1D (depth-integrated) and cannot capture any effects perpendicular to the channel direction. Visual inspection of the experiments suggests that there is not pronounced cross-channel flow. Our channel width, at 15 cm, is larger than that used by Balmforth et al. [40] who find a 10 cm channel outperforms a 5 cm channel. We estimate the boundary layer width for a Herschel-Bulkley fluid, $\delta = \left(\frac{(1+1/n)^n K U^n H}{\tau_y} \right)^{n/(n+1)}$ [61] at high Bingham number ($Bi =$

$\frac{\tau_y}{K} \left(\frac{U}{\delta} \right)^{-n}$), where U is the maximum velocity along the channel, and scales with the height of the flow at low Bingham number. Our experiments fall in the intermediate Bingham number range, and we expect boundary layer thicknesses between <1 cm and 17.5 cm. Experiments with boundary layers larger than half the channel width (8.5 cm) are noted in Table S2. The misfits between these experiments and the model do not show systematic differences nor are the misfits different in magnitude compared to experiments with low predicted boundary layer thicknesses.

The uncertainties on the values for K_r , τ_y , and n we derive from inversion of the experimental data are 25%, 31%, and 14%, respectively, and the mismatch with models for those parameters (Eqs 4.1a–4.1c) are 35%, 106%, and 10%. Our experiments show good repeatability at $\phi_{gas} \leq 0.6$. If we compare experiments for which ϕ_{solid} and ϕ_{gas} are within $\pm 5\%$, and de-trended K_r , τ_y , and n values using their respective models, we find ranges of 38%, 149%, and 20% in those parameters, which are of the same order as uncertainties and mismatch. For $\phi_{gas} > 0.6$, the data show greater variability with ranges of 68%, 154%, and 73%, respectively. Data variability may be related to experimental sources of uncertainty, such as small errors in flow density or height of fluid in the reservoir to which the forward model is very sensitive, or microstructural differences in the particle and bubble populations. Yield stress measurements at all bubble fractions show scatter between experiments and misfit to the model higher than the uncertainty predicted by EnKF model fitting, which may come from real variation among samples rather than trade-offs between fitting parameters.

We see consistent deviations between the experimental data and the rheology model in the range of $\phi_{gas} > 0.6$, where the model consistently over-predicts both the relative consistency and flow index, perhaps due to trade-offs in the inversion of the experimental data. To test the importance of trade-offs in fitting parameters, we find the Pearson correlation coefficients between the EnKF instances after the final propagation (best fit for the fitting parameters) for each experiment. A value of 1 indicates a perfect positive correlation, -1 a perfect negative correlation, and 0 no correlation. The EnKF analyses reveal a moderate correlation between the slope angle and consistency, with an average correlation coefficient between EnKF samples for each experiment of $C=0.63$. We also find weak correlations between slope angle and yield stress ($C=0.25$) and slope angle and flow index ($C=-0.44$); a weak positive correlation between consistency and flow index in experiments with $\phi_{gas} > 0.6$ ($C=0.27$); a moderate negative correlation when $\phi_{gas} < 0.2$ ($C=-0.40$); and no apparent correlation at intermediate gas volume fractions $0.2 < \phi_{gas} < 0.6$ ($C=-0.01$). We do not observe correlations in the parameter inversions between yield stress and consistency ($C=-0.06$) or yield stress and flow index ($C=0.11$). For an example of the EnKF inversion results and match to experimental data see Supplementary Fig. S5.

Our results consider strain rates up to 10^1 1/s and maximum Ca between $\approx 10^{-2}$ and 10^1 . We find that bubbles lead to a higher effective viscosity than predicted by the Cross model [1], but our experiments do not cover a large-enough range of Ca to comment on asymptotic behavior that may occur at much higher or lower Ca . Given the strong strain-rate dependence of the Herschel–Bulkley formulation, this model may not be appropriate for fluids experiencing strain rates far outside the calibration region ($\gg 10$ 1/s) as may occur in natural settings, including during conduit ascent in explosive eruptions or in fast-moving lava flows.

Additional uncertainty exists for the estimate of Ca , which is difficult to define for a polydisperse bubble population whose exact bubble sizes and deformation cannot be directly observed. Estimates for the bubble size distribution are available in the supplementary material. Bubble deformation is observed for some of the largest bubbles experiencing the strongest shear, and thus experiencing the highest Ca conditions, imaged through the side walls of the channel (Supplementary Fig. S2). Such observations are limited to the exterior of the flow, which is necessarily dominated by edge effects. Better characterization of bubble sizes and deformations in the flow interior is an avenue for future work.

(c) Application to lava dynamics

We demonstrate the implications of our new three-phase suspension rheology model with realistic parameters for lava flows through implementation to the channelized lava flow model PyFLOWGO [62, 63]. PyFLOWGO is a 1D lava flow advance model for the velocity and final runout distance of a cooling and crystallizing lava. The physical model uses a Bingham-plastic rheology of the form $\tau = \tau_y + \eta_{eff}\dot{\gamma}$. We add our experimentally constrained rheology model to several built-in parameterizations for the yield stress and effective viscosity. We calculate τ_y using Eq. 3b and the effective viscosity term $\eta_{eff} = K_r\mu\dot{\gamma}^{n-1}$ using Eqs. 3a and 3c. We compare our model with the commonly used two-phase modified Einstein-Roscoe relationship [46], and three-phase model of Phan-Thien and Pham [16].

We take the flow simulation parameters from the well-documented LSF1 lava flow from Mount Etna, Italy in 2001. We initiate the simulated lava with a low solid volume fraction of $\phi_{solid} = 0.1$. Solid fraction then increases, with further crystallization during emplacement, to $\phi_{solid} = 0.15$ when using our rheological relations, and $\phi_{solid} = 0.3$ for the modified Einstein-Roscoe and Phan-Thien and Pham [16] relationships. Gas fraction begins and remains at $\phi_{gas} = 0.65$. The simulated flow follows the path of steepest descent in the pre-eruptive topography. The initial flux is 20 m³/s. We use a temperature-dependent melt viscosity using the VFT equation ($a = -4.827$, $b = 5997$, $c = -330.3$) [64, 65, 66]. We tune the model parameters of initial channel width (set to 40 m) and temperature (set to 1223.15 K) to obtain the observed flow height (10 m) and mean velocity (10^{-3} to 4×10^{-2} m/s) when using our new rheology model. The width and initial temperature are held constant across all simulations. To predict the effective viscosity, we use a reference strain rate of 10^{-3} s⁻¹ for this lava flow, estimated from observed velocities and flow thickness. We approximate the shear rate dependence using the capillary number calculated for a 1 cm radius bubble and a surface tension of air in basalt of 0.37 N/m [29]. As the flow cools, the melt viscosity, crystal content, and effective bulk viscosity are updated every step.

Our model predicts a higher effective viscosity compared to that of Phan-Thien and Pham [16] or Roscoe [46] by more than an order of magnitude, and yields a mean velocity that is ~ 3 times slower (Fig. 4). Additionally, our yield strength model diverges from that based on Dragoni [67] ~ 80 m down flow, when the crystal fraction increases enough to support significant bubble-crystal interactions. Although shear-thinning behavior is not included in PyFLOWGO, we compare effective viscosities predicted by our model assuming a Bingham-plastic rheology ($n = 1$) and with a dynamic value for n in response to changing crystal fraction (while maintaining a constant shear rate). We highlight that for the large bubble volume fraction of some natural lavas, n deviates from one (initially $n \approx 0.82$) and can result in a factor of two difference in effective viscosity, and a 15% difference in runout distance. This effect may be more pronounced in modeling that includes a physical model for shear-rate dependence in the flow.

6. Conclusion

We use a dam-break setup to measure the rheology of three-phase suspensions, scaled to apply to magma and lava. Through the use of a chemical reaction between baking soda and citric acid, we are able to create corn syrup suspensions with bubble volume fractions up to 0.82 and particle volume fractions up to 0.37. Strain rates in our experiments range up to 10^1 1/s and maximum Ca between $\approx 10^{-2}$ and 10^1 , relevant to basaltic lava flows. We invert for a Herschel–Bulkley rheology using a depth-integrated 1D forward model [39] and the probabilistic Ensemble Kalman Filter approach.

Based on our results, we develop a suite of models for the Herschel–Bulkley parameters, calibrated across the whole dataset, which are presented in equations 4.1a–4.1c. Combined with equation 2.3, this constitutes a rheological model for three phase suspensions. Our results show good agreement with existing literature for particle-bearing suspensions with a strongly non-linear increase in viscosity with increasing particle fraction, development of yield stresses at particle fractions $\phi_{solid} \gtrsim 0.35$, and development of shear-thinning behavior at particle fractions

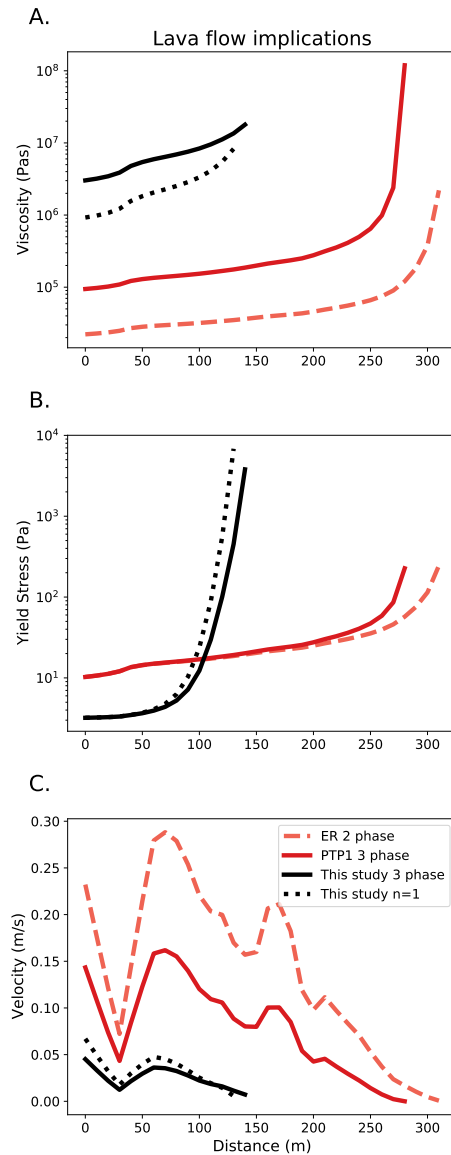


Figure 4. Implications of the experimentally determined three-phase rheology on predictions of lava flows. Our model results in a higher relative effective viscosity (A), a sharper increase in yield stress as particle-bubble interactions become important (B), and lower mean velocity (C) compared to the models of Roscoe [46] (two-phase) or Phan-Thien and Pham [16] (three-phase). We also highlight the contrast between assuming $n=1$ (Bingham-plastic rheology) and the Herschel-Bulkley rheology ($n \approx 0.8$) that results in a decrease in effective viscosity by a factor of 2 at low crystal fractions.

$\phi_{solid} \gtrsim 0.39$. Our findings indicate that suspended gas leads to a non-linear increase in viscosity with increasing bubble fraction, larger than predicted by previous work, and development of yield stresses and shear rate-dependent behavior at bubble fractions, or combined bubble and particle fractions, similar to those observed for particle-only suspensions. We find that shear-rate dependence of bubble-bearing two- and three-phase suspensions are shear thinning in the low capillary number regime and become shear thickening with increasing capillary number. This

study contributes an explicit incorporation of three-phase interactions into a novel model for yield stress, and a parameterization for the inclusion of capillary number in flow index.

We highlight the implications of our model for magma/lava dynamics through application to the lava flow emplacement model PyFLOWGO, and show higher viscosities and lower predicted velocities for surface lava flows as a result of the stiffening behavior of concentrated bubble suspensions at low and intermediate capillary numbers. Our findings underscore the need to incorporate three-phase rheology into simulations of magma or lava flow used to address fundamental science questions as well as hazard assessment and mitigation.

Data Accessibility. Experiment videos available at <https://doi.org/10.5281/zenodo.4685257>. data processing code available at <https://doi.org/10.5281/zenodo.4707969> or <https://github.com/JanineBirnbaum18/3-phase-flow>.

Authors' Contributions. J.B. carried out the experiments and data analysis. E.L. conceived of and supervised the experiments and data analysis. E.W.L. contributed to the interpretation of the results. J.B. took the lead in writing the manuscript. All authors provided critical feedback and helped shape the research, analysis and manuscript.

Competing Interests. The authors have no competing interests to declare.

Funding. This work was supported by NSF under awards NSF EAR-1654588 and NSF EAR-1929008, and by NERC under award NE/T009594/1.

Acknowledgements. We thank J. Hammer and A. Whittington for their constructive comments, and Lamont-Doherty's Secondary School Field Research Program participants R. Burgos, M. Diakite, and L. Lyons for their assistance in conducting experiments. We thank two anonymous reviewers for their constructive suggestions which helped improve and clarify the manuscript.

References

- 1 H M Mader, E W Llewellyn, and S P Mueller. The rheology of two-phase magmas: A review and analysis. *Journal of Volcanology and Geothermal Research*, 257:135–158, 2013. ISSN 0377-0273. doi: 10.1016/j.jvolgeores.2013.02.014. URL <http://dx.doi.org/10.1016/j.jvolgeores.2013.02.014>.
- 2 A Einstein. Berichtigung zu meiner Arbeit: Eine neue Bestimmung der Moleküldimensionen. *Annalen der Physik*, 339(3):591–592, 1 1911. doi: 10.1002/andp.19113390313.
- 3 Irvin M. Krieger and Thomas J. Dougherty. A Mechanism for Non-Newtonian Flow in Suspensions of Rigid Spheres. *Transactions of the Society of Rheology*, 3(1):137–152, 1959. ISSN 0038-0032. doi: 10.1122/1.548848. URL <http://sor.scitation.org/doi/10.1122/1.548848>.
- 4 S. Mueller, E W Llewellyn, and H. M. Mader. The rheology of suspensions of solid particles. *Proceedings of the Royal Society A: Mathematical, Physical and Engineering Sciences*, 466(2116): 1201–1228, 2010. ISSN 0303402X. doi: 10.1007/BF01432034.
- 5 A. K.S. Chesterton, D. A.Pereira De Abreu, G. D. Moggridge, P. A. Sadd, and D. I. Wilson. Evolution of cake batter bubble structure and rheology during planetary mixing. *Food and Bioproducts Processing*, 91(3):192–206, 2013. ISSN 09603085. doi: 10.1016/j.fbp.2012.09.005. URL <http://dx.doi.org/10.1016/j.fbp.2012.09.005>.
- 6 E. W. Llewellyn, H. M. Mader, and S. D. R. Wilson. The constitutive equation and flow dynamics of bubbly magmas. *Geophysical Research Letters*, 29(24), 2002. ISSN 00948276. doi: 10.1029/2002gl015697.
- 7 E. W. Llewellyn and M. Manga. Bubble suspension rheology and implications for conduit flow. *Journal of Volcanology and Geothermal Research*, 143:205–217, 2005. ISSN 03770273. doi: 10.1016/j.jvolgeores.2004.09.018.
- 8 Michael Manga, Jonathan Castro, Katharine V Cashman, and Michael Loewenberg. Rheology of bubble-bearing magmas. *Journal of Volcanology and Geothermal Research*, 87(1-4):15–28, 1998. ISSN 0012821X. doi: 10.1016/S0012-821X(98)00278-7.
- 9 Rajinder Pal. Rheological behavior of bubble-bearing magmas. *Earth and Planetary Science Letters*, 207(1-4):165–179, 2003. ISSN 0012821X. doi: 10.1016/S0012-821X(02)01104-4.

- 10 Mattia Pistone, Luca Caricchi, Peter Ulmer, Luigi Burlini, Paola Ardia, Eric Reusser, Federica Marone, and Laurent Arbaret. Deformation experiments of bubble- and crystal-bearing magmas: Rheological and microstructural analysis. *Journal of Geophysical Research*, 117, 2012. doi: 10.1029/2011JB008986.
- 11 H. M. Princen and A. D. Kiss. Rheology of foams and highly concentrated emulsions: IV. An experimental study of the shear viscosity and yield stress of concentrated emulsions. *Journal of Colloid and Interface Science*, 128(1):176–187, 1989. ISSN 18790399. doi: 10.1016/j.cocis.2014.11.003.
- 12 Florence Rouyer, Sylvie Cohen-Addad, and Reinhard Höhler. Is the yield stress of aqueous foam a well-defined quantity? *Colloids and Surfaces A: Physicochemical and Engineering Aspects*, 263:111–116, 2005. ISSN 09277757. doi: 10.1016/j.colsurfa.2005.01.025.
- 13 A. C. Rust and Michael Manga. Effects of bubble deformation on the viscosity of dilute suspensions. *Journal of Non-Newtonian Fluid Mechanics*, 104(1):53–63, 2002. ISSN 03770257. doi: 10.1016/S0377-0257(02)00013-7.
- 14 Daniel J. Stein and Frank J. Spera. Rheology and microstructure of magmatic emulsions: theory and experiments. *Journal of Volcanology and Geothermal Research*, 49:157–174, 1992. ISSN 03770273. doi: 10.1016/0377-0273(92)90011-2.
- 15 G. I. Taylor. The viscosity of a fluid containing small drops of another fluid. *Proceedings of the Royal Society of London. Series A, Containing Papers of a Mathematical and Physical Character*, 138(834):41–48, 10 1932. ISSN 0950-1207. doi: 10.1098/rspa.1932.0169. URL <https://royalsocietypublishing.org/doi/10.1098/rspa.1932.0169>.
- 16 N. Phan-Thien and D. C. Pham. Differential multiphase models for polydispersed suspensions and particulate solids. *Journal of Non-Newtonian Fluid Mechanics*, 72:305–318, 1997. ISSN 03770257. doi: 10.1016/S0377-0257(97)90002-1.
- 17 J. M. Truby, S. P. Mueller, E. W. Llewellyn, and H. M. Mader. The rheology of three-phase suspensions at low bubble capillary number. *Proceedings of the Royal Society A: Mathematical, Physical and Engineering Sciences*, 471(2173), 2015. ISSN 14712946. doi: 10.1098/rspa.2014.0557.
- 18 Donald B. Dingwell and Sharon L. Webb. Structural relaxation in silicate melts and non-Newtonian melt rheology in geologic processes. *Physics and Chemistry of Minerals*, 16(5): 508–516, 1989. ISSN 03421791. doi: 10.1007/BF00197020.
- 19 Daniele Giordano, James K Russell, and Donald B Dingwell. Viscosity of magmatic liquids : A model. *Earth and Planetary Science Letters*, 271:123–134, 2008. doi: 10.1016/j.epsl.2008.03.038.
- 20 Helge M. Gonnermann and Michael Manga. The fluid mechanics inside a volcano. *Annual Review of Fluid Mechanics*, 39:321–356, 2007. ISSN 00664189. doi: 10.1146/annurev.fluid.39.050905.110207.
- 21 Katharine V. Cashman and R. Stephen J. Sparks. How volcanoes work: A 25 year perspective. *Bulletin of the Geological Society of America*, 125(5-6):664–690, 2013. ISSN 00167606. doi: 10.1130/B30720.1.
- 22 F. J. Ryerson, H. C. Weed, and A. J. Piwinski. Rheology of subliquidus magmas. 1. Picritic compositions. *Journal of Geophysical Research*, 93(B4):3421–3436, 1988. ISSN 01480227. doi: 10.1029/JB093iB04p03421.
- 23 Harry Pinkerton and Gill Norton. Rheological properties of basaltic lavas at sub-liquidus temperatures: laboratory and field measurements on lavas from Mount Etna. *Journal of Volcanology and Geothermal Research*, 68(4):307–323, 1995. ISSN 03770273. doi: 10.1016/0377-0273(95)00018-7.
- 24 Hidemi Ishibashi. Non-Newtonian behavior of plagioclase-bearing basaltic magma: Subliquidus viscosity measurement of the 1707 basalt of Fuji volcano, Japan. *Journal of Volcanology and Geothermal Research*, 181:78–88, 2009. ISSN 03770273. doi: 10.1016/j.jvolgeores.2009.01.004. URL <http://dx.doi.org/10.1016/j.jvolgeores.2009.01.004>.
- 25 A. Soldati, A. Sehlke, G. Chigna, and A. Whittington. Field and experimental constraints on the rheology of arc basaltic lavas: the January 2014 Eruption of Pacaya (Guatemala). *Bulletin of Volcanology*, 78(6), 2016. ISSN 14320819. doi: 10.1007/s00445-016-1031-6. URL <http://dx.doi.org/10.1007/s00445-016-1031-6>.
- 26 Angelo Castruccio, A. C. Rust, and R. S.J. Sparks. Rheology and flow of crystal-bearing lavas: Insights from analogue gravity currents. *Earth and Planetary Science Letters*, 297:471–480, 2010.

- ISSN 0012821X. doi: 10.1016/j.epsl.2010.06.051. URL <http://dx.doi.org/10.1016/j.epsl.2010.06.051>.
- 27 Nikolai Bagdassarov, Alexander Dorfman, and Donald B. Dingwell. Effect of alkalis, phosphorus, and water on the surface tension of haplogranite melt. *American Mineralogist*, 85:33–40, 2000. ISSN 0003004X. doi: 10.2138/am-2000-0105.
 - 28 Margaret Mangan and Thomas Sisson. Evolution of melt-vapor surface tension in silicic volcanic systems: Experiments with hydrous melts. *Journal of Geophysical Research: Solid Earth*, 110:1–9, 2005. ISSN 21699356. doi: 10.1029/2004JB003215.
 - 29 D Walker and O Mullins. Surface Tension of Natural Silicate Melts from 1,200°–1,500°C and Implications for Melt Structure. *Contributions to Mineralogy and Petrology*, 76(4):455–462, 1981. doi: 10.1007/BF00371487.
 - 30 N. Petford, M. A. Koenders, and J. D. Clemens. Igneous differentiation by deformation. *Contributions to Mineralogy and Petrology*, 175:1–21, 2020. ISSN 14320967. doi: 10.1007/s00410-020-1674-3. URL <https://doi.org/10.1007/s00410-020-1674-3>.
 - 31 Sylvie Vergnolle. Bubble size distribution in magma chambers and dynamics of basaltic eruptions. *Earth and Planetary Science Letters*, 140:269–279, 1996. ISSN 0012821X. doi: 10.1016/0012-821X(96)00042-8.
 - 32 I. Galindo and A. Gudmundsson. Basaltic feeder dykes in rift zones: Geometry, emplacement, and effusion rates. *Natural Hazards and Earth System Science*, 12:3683–3700, 2012. ISSN 15618633. doi: 10.5194/nhess-12-3683-2012.
 - 33 Hélène Gaonac’h, Shaun Lovejoy, and Daniel Schertzer. Scaling vesicle distributions and volcanic eruptions. *Bulletin of Volcanology*, 67(4):350–357, 2005. ISSN 02588900. doi: 10.1007/s00445-004-0376-4.
 - 34 Simon Thivet, Lucia Gurioli, and Andrea Di Muro. Basaltic dyke eruptions at Piton de La Fournaise: characterization of the eruptive products with implications for reservoir conditions, conduit processes and eruptive dynamics. *Contributions to Mineralogy and Petrology*, 175:1–24, 2020. ISSN 14320967. doi: 10.1007/s00410-020-1664-5. URL <https://doi.org/10.1007/s00410-020-1664-5>.
 - 35 Heather L. Petcovic and Josef D. Dufek. Modeling magma flow and cooling in dikes: Implications for emplacement of Columbia River flood basalts. *Journal of Geophysical Research: Solid Earth*, 110(B10201):1–15, 2005. ISSN 21699356. doi: 10.1029/2004JB003432.
 - 36 Winslow H Herschel and R Bulkley. Konsistenzmessungen von Gummi-Benzollösungen. *Kolloid Zeitschrift*, 39:291, 1926.
 - 37 A. C. Rust and Michael Manga. Bubble shapes and orientations in low Re simple shear flow. *Journal of Colloid and Interface Science*, 249(2):476–480, 2002. ISSN 00219797. doi: 10.1006/jcis.2002.8292.
 - 38 D. E. Sinat-Radchenko. No Title. *Sakharnaia Promyshlennost*, 3:28–31, 1982.
 - 39 Ko Fei Liu and Chiang C. Mei. Slow spreading of a sheet of Bingham fluid on an inclined plane. *Journal of Fluid Mechanics*, 207:505–529, 1989. ISSN 14697645. doi: 10.1017/S0022112089002685.
 - 40 N. J. Balmforth, R. V. Craster, P. Perona, A. C. Rust, and R. Sassi. Viscoplastic dam breaks and the Bostwick consistometer. *Journal of Non-Newtonian Fluid Mechanics*, 142(1-3):63–78, 2007. ISSN 03770257. doi: 10.1016/j.jnnfm.2006.06.005.
 - 41 K. Madlener, B. Frey, and H. K. Ciezki. Generalized Reynolds number for non-Newtonian fluids. *Progress in Propulsion Physics*, 1:237–250, 2009. doi: 10.1051/eucass/200901237.
 - 42 Pierre-Gilles de Gennes, Françoise Brochard-Wyart, and David Quéré. *Capillarity and Wetting Phenomena*. Springer New York, New York, NY, 2004. ISBN 978-1-4419-1833-8. doi: 10.1007/978-0-387-21656-0. URL <http://link.springer.com/10.1007/978-0-387-21656-0>.
 - 43 Patricia M. Gregg and J. Cory Pettijohn. A multi-data stream assimilation framework for the assessment of volcanic unrest. *Journal of Volcanology and Geothermal Research*, 309:63–77, 2016. ISSN 03770273. doi: 10.1016/j.jvolgeores.2015.11.008. URL <http://dx.doi.org/10.1016/j.jvolgeores.2015.11.008>.
 - 44 Yan Zhan and Patricia M. Gregg. Data assimilation strategies for volcano geodesy. *Journal of Volcanology and Geothermal Research*, 344:13–25, 2017. ISSN 03770273. doi: 10.1016/j.jvolgeores.2017.02.015. URL <http://dx.doi.org/10.1016/j.jvolgeores.2017.02.015>.

- 45 R H Byrd, P Lu, and J Nocedal. A Limited Memory Algorithm for Bound Constrained Optimization. *SIAM Journal on Scientific and Statistical Computing*, 16(5):1190–1208, 1995.
- 46 R. Roscoe. The viscosity of suspensions of rigid spheres. *British Journal of Applied Physics*, 3: 267–269, 1952. ISSN 05083443. doi: 10.1088/0508-3443/3/8/306.
- 47 Antonio Costa, Luca Caricchi, and Nickolai Bagdassarov. A model for the rheology of particle-bearing suspensions and partially molten rocks. *Geochemistry, Geophysics, Geosystems*, 10(3), 2009. doi: 10.1029/2008GC002138.
- 48 M. Mooney. The viscosity of a concentrated suspension of spherical particles. *Journal of Colloid Science*, 6(2):162–170, 1951. ISSN 00958522. doi: 10.1016/0095-8522(51)90036-0.
- 49 S R Hoover, K V Cashman, and M Manga. The yield strength of subliquidus basalts - experimental results. *Journal of Volcanology and Geothermal Research*, 107:1–18, 2001. URL papers://bcab5980-e9b6-4eaf-b643-294662106260/Paper/p935.
- 50 P. Coussot. Yield stress fluid flows: A review of experimental data. *Journal of Non-Newtonian Fluid Mechanics*, 211:31–49, 2014. ISSN 03770257. doi: 10.1016/j.jnnfm.2014.05.006. URL <http://dx.doi.org/10.1016/j.jnnfm.2014.05.006>.
- 51 A. J. Hogg and G. P. Matson. Slumps of viscoplastic fluids on slopes. *Journal of Non-Newtonian Fluid Mechanics*, 158:101–112, 2009. ISSN 03770257. doi: 10.1016/j.jnnfm.2008.07.003.
- 52 Christophe Ancey and Steve Cochard. The dam-break problem for Herschel-Bulkley viscoplastic fluids down steep flumes. *Journal of Non-Newtonian Fluid Mechanics*, 158:18–35, 2009. ISSN 03770257. doi: 10.1016/j.jnnfm.2008.08.008.
- 53 Xin Huang and Marcelo H. García. A Herschel-Bulkley model for mud flow down a slope. *Journal of Fluid Mechanics*, 374:305–333, 1998. ISSN 00221120. doi: 10.1017/S0022112098002845.
- 54 Didier Vola, F. Babik, and J. C. Latché. On a numerical strategy to compute gravity currents of non-Newtonian fluids. *Journal of Computational Physics*, 201(2):397–420, 2004. ISSN 00219991. doi: 10.1016/j.jcp.2004.05.019.
- 55 C. Ancey, N. Andreini, and G. Epely-Chauvin. Viscoplastic dambreak waves: Review of simple computational approaches and comparison with experiments. *Advances in Water Resources*, 48: 79–91, 2012. ISSN 03091708. doi: 10.1016/j.advwatres.2012.03.015. URL <http://dx.doi.org/10.1016/j.advwatres.2012.03.015>.
- 56 Nicolas Andreini, Gaël Epely-Chauvin, and Christophe Ancey. Internal dynamics of Newtonian and viscoplastic fluid avalanches down a sloping bed. *Physics of Fluids*, 24(5):1–20, 2012. ISSN 10706631. doi: 10.1063/1.4718018.
- 57 Alessandro Cantelli. Uniform Flow of Modified Bingham Fluids in Narrow Cross Sections. *Journal of Hydraulic Engineering*, 135(8):640–650, 2009. ISSN 0733-9429. doi: 10.1061/(asce)hy.1943-7900.0000092.
- 58 Guillaume Chambon, A. Ghemmour, and M. Naaim. Experimental investigation of viscoplastic free-surface flows in a steady uniform regime. *Journal of Fluid Mechanics*, 754: 332–364, 2014. ISSN 14697645. doi: 10.1017/jfm.2014.378.
- 59 S. Cochard and C. Ancey. Experimental investigation of the spreading of viscoplastic fluids on inclined planes. *Journal of Non-Newtonian Fluid Mechanics*, 158:73–84, 2009. ISSN 03770257. doi: 10.1016/j.jnnfm.2008.08.007.
- 60 S. Longo, L. Chiapponi, and V. Di Federico. On the propagation of viscous gravity currents of non-Newtonian fluids in channels with varying cross section and inclination. *Journal of Non-Newtonian Fluid Mechanics*, 235:95–108, 2016. ISSN 03770257. doi: 10.1016/j.jnnfm.2016.07.007.
- 61 J. Boujlel, M. Maillard, A. Lindner, G. Ovarlez, X. Chateau, and P. Coussot. Boundary layer in pastes—Displacement of a long object through a yield stress fluid. *Journal of Rheology*, 56: 1083–1108, 2012. ISSN 0148-6055. doi: 10.1122/1.4720387.
- 62 A. J. L. Harris and Scott K. Rowland. FLOWGO: a kinematic thermo-rheological model for lava cooling in a channel, 2001.
- 63 Magdalena Oryaëlle Chevrel, Jérémie Labroquère, Andrew J.L. Harris, and Scott K. Rowland. PyFLOWGO: An open-source platform for simulation of channelized lava thermo-rheological properties. *Computers and Geosciences*, 111:167–180, 2018. ISSN 00983004. doi: 10.1016/j.cageo.2017.11.009.

- 64 B Cordonnier, E Lev, and F Garel. Benchmarking lava-flow models. *The Geological Society of London*, 426:425–445, 2016. doi: <https://doi.org/10.1144/SP426.7>.
- 65 M. Coltelli, C. Proietti, S. Branca, Maria Marsella, D. Andronico, and L. Lodato. Analysis of the 2001 lava flow eruption of Mt. Etna from three-dimensional mapping. *Journal of Geophysical Research: Earth Surface*, 112:1–18, 2007. ISSN 21699011. doi: 10.1029/2006JF000598.
- 66 V. Lombardo and M. F. Buongiorno. Lava flow thermal analysis using three infrared bands of remote-sensing imagery: A study case from Mount Etna 2001 eruption. *Remote Sensing of Environment*, 101:141–149, 2006. ISSN 00344257. doi: 10.1016/j.rse.2005.12.008.
- 67 Michele Dragoni. A dynamical model of lava flows cooling by radiation. *Bulletin of Volcanology*, 51(2):88–95, 1989. ISSN 02588900. doi: 10.1007/BF01081978.

Supplementary Material

7. Supplementary Material

(a) Supplementary figure descriptions

We characterize the bubble size distributions of our experiments using optical imaging at two different spatial scales. First, we consider the smallest size fraction of bubbles in undeformed syrup suspensions using optical microscopy which allows us to resolve bubbles between $20\ \mu\text{m}$ and $2\ \text{mm}$ in diameter. Second, we characterize the size distribution and shear-induced elongation of bubbles $\gtrsim 1.5\ \text{mm}$ that are visible without magnification through the walls of the clear channel.

The smallest bubble size fractions are determined from photomicrographs analyzed using a MATLAB circle-finding algorithm and FOAMS (Shea et al. 2010). Results show a power-law distribution of bubble number density, shown in Fig. S1 for an undeformed sample with only gas suspended in liquid (no solids). In the presence of particles, heterogeneous nucleation is observed with small bubbles ($\lesssim 50\ \mu\text{m}$ in diameter) nucleating and growing on the uneven surfaces of the particles. This population shows greater spatial heterogeneity, obvious in panel B of Fig. S1 in which a region with fewer particles shows fewer and larger bubbles, while an adjacent area shows a greater density of small bubbles. The high density of bubbles on the particle surfaces introduce significant errors to the size distribution estimate for three-phase suspensions, making quantitative comparison challenging. We might additionally expect the population size to vary in response to shear, but deformation and coalescence at this size fraction are hindered by the relatively high surface tension.

To characterize the larger bubbles visible through the side walls of the channel, we again utilize FOAMS (Shea et al. 2010) to calculate bubble volume, aspect ratio, and elongation direction distributions. We compare the bubbles found in the undeformed reservoir with the flow front after 8 min to show a change in the elongation direction of large bubbles (Fig. S2). The reservoir and the flow front show similar size distributions with a logarithmic decrease in bubble number density with increasing size at a comparable rate to the smaller size fraction (measured on two different sample suspensions). Both populations show slight elongations (mean aspect ratio ≈ 0.6), but the bubbles in the reservoir show a preferential vertical orientation as bubbles rise due to buoyancy, while the bubbles at the flow front are aligned with the flow direction, an approximately 90° rotation.

We also add a photograph in Fig. S3 taken from the underside of the channel looking up at the flow. It shows bubbles in contact with the bottom of the channel, without the formation of a segregated bubble-free layer.

Fig. S4 shows the relative error between experiments and the empirical model, normalized by the experimental results. We also include an example experiment inversion including the posterior distributions of $K_r, \tau_y, n,$ and θ which show strong covariance between the slope and relative consistency, a good fit between observations and the maximum likelihood model, and convergence of the EnKF inversion after 3 iterations. Finally, we report each relationship shown in Fig. 3. Fig S5 shows a typical example of inversion results for a flow including A.) the posterior distributions and covariations between rheological parameters (K_r, τ_y, n) and slope (θ); B.) the flow front propagation of the experiment (red) and model (blue) with confidence bounds from forward models using the 5th and 95th quantiles of the posterior distributions; and C.) the convergence of the EnKF inversion. Supplementary references T. Shea, B. F. Houghton, L. Gurioli, K. V. Cashman, J. E. Hammer, B. J. Hobden (2010). Textural studies of vesicles in volcanic rocks: An integrated methodology. J. Volcanol. Geotherm. Res. 190, 271–289.

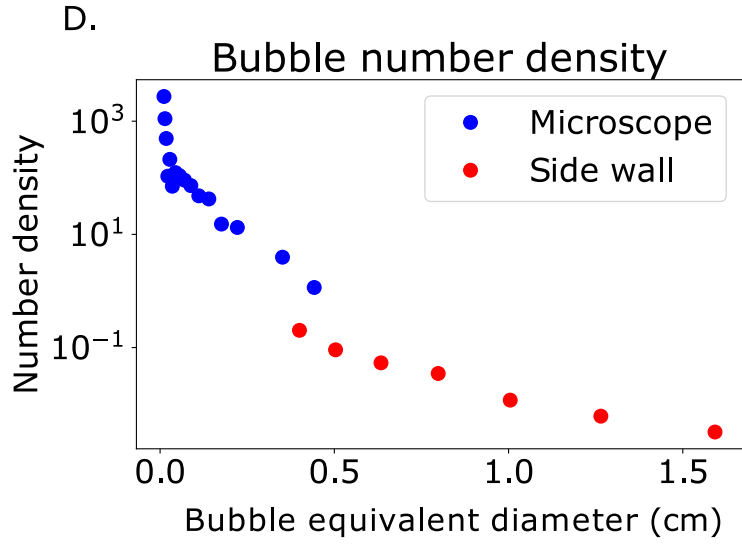
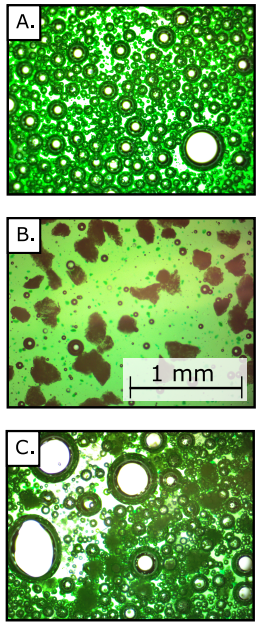


Figure S1. Photomicrographs of A) bubbles, B) particles, and C) both bubbles and particles. Note the change in size distribution between the left and right sides of C) as a result of small-scale heterogeneities in particle distribution. D) Summarizes the bubble number density of representative solutions where small bubbles were characterized under the microscope and large bubbles were identified optically through the clear sides of the channel.

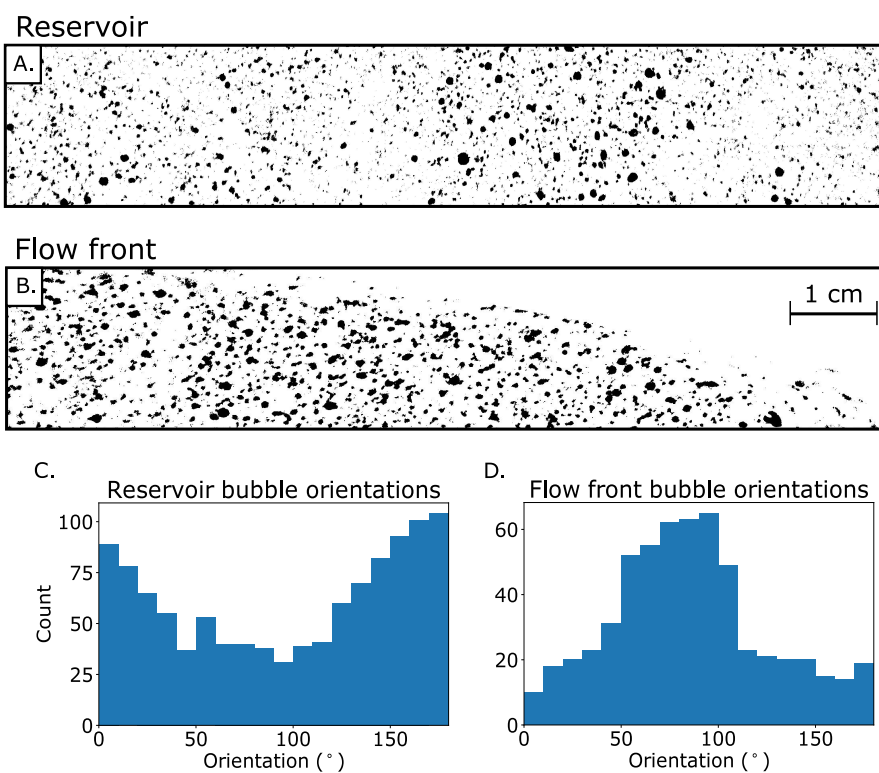


Figure S2. Binary images of bubbles (black) suspended in syrup (white) as seen through the clear channel walls in the A) undeformed fluid reservoir, and B) the flow front of the same flow. A) and B) share the same scale. C) and D) show the respective bubble elongation orientations, highlighting a 90° rotation from vertically-deformed bubbles (C) to bubbles aligned with horizontal flow to the right (D).



Figure S3. View of an example flow from below showing bubbles in contact with the bottom of the channel. Bubbles do not show preferred orientation in the direction of flow, consistent with a no-slip condition at the base of the flow.

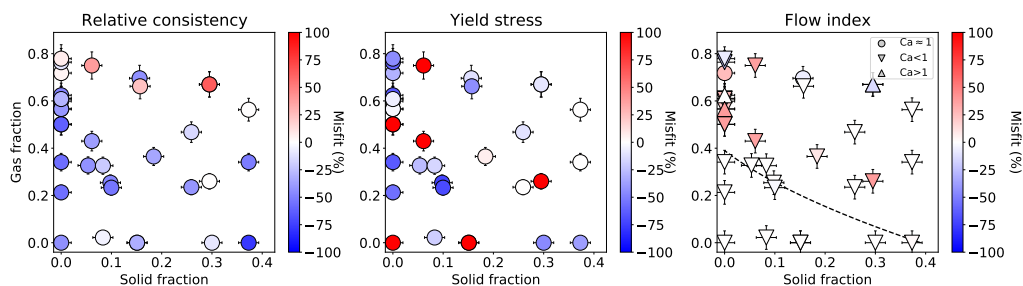


Figure S4. Relative misfit between experimental measurements for rheological parameters and best-fit model for A) relative consistency, K , B) yield stress, τ_{ij} , and C) flow index, n .

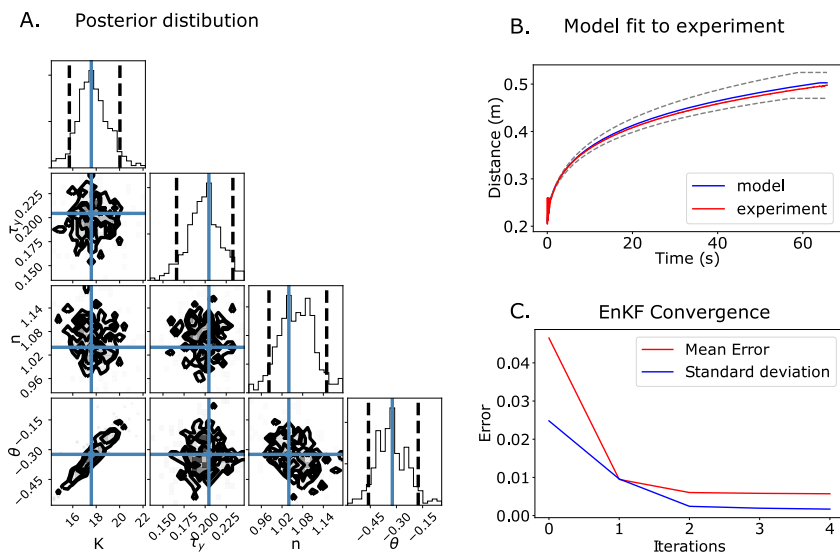


Figure S5. Representative Ensemble Kalman Filter (EnKF) inversion. A) shows a corner plot of the posterior distribution that highlight the covariation between pairs of parameters, most clearly the relationship between relative consistency and slope. B) forward model of best fit parameters (blue) and experimental data (red), with confidence intervals (dashed grey). C) EnKF convergence with 300 ensembles over five iterations.

Video	Temp (°C)	Height (m)	Syrup visc (Pas)	Density (kg/m ³)	Solid	Gas	Max bubble radius (m)	Max strain rate (1/s)	Capillary number	Relative consistency	Error (%)	Yield stress (Pa)	Error (%)	Flow index	Error (%)	Boundary-layer thickness (m)
MVL0006	28.8	0.095	4.29	535	0	0.61	0.006	1.16	0.40	13.27 ± 1.29	-39.37	7.03 ± 1.28	-39.03	0.96 ± 0.05	0	0.057
MVL0007	22.3	0.042	8.00	874	0.30	0.67	0.007	5.32	3.46	47.76 ± 1.54	31.39	16.96 ± 2.07	0	1.14 ± 0.10	18.95	0.006
MVL0010	23.4	0.100	7.12	458	0.30	0.67	0.007	1.83	1.20	40.61 ± 4.33	63.49	22.48 ± 2.28	-9.64	1.27 ± 0.07	-14.21	0.009
MVL0011	23.9	0.041	6.76	1028	0.30	0.26	0.002	3.11	0.58	14.76 ± 1.25	0	0.31 ± 0.05	709.93	0.66 ± 0.05	38.90	0.041
MVL0012	24.2	0.110	6.56	351	0.06	0.75	0.003	2.05	0.44	14.98 ± 0.69	38.66	3.30 ± 0.35	134.46	0.57 ± 0.05	37.01	0.110*
MVL0013	24.4	0.055	6.43	794	0.06	0.43	0.002	4.92	0.79	8.28 ± 0.98	-37.95	0.27 ± 0.04	569.50	0.68 ± 0.06	36.24	0.055
MVL0703	28.4	0.060	4.44	696	0	0.5	0.005	1.26	0.33	11.36 ± 0.93	-47.81	6.22 ± 1.07	-54.17	0.90 ± 0.07	0	0.071
MVL0707	30.1	0.052	3.85	697	0	0.5	0.003	1.50	0.18	13.13 ± 1.83	-62.32	0.70 ± 0.13	162.54	0.64 ± 0.05	37.93	0.052
MVL0708	30.5	0.051	3.73	605	0	0.57	0.004	1.50	0.27	12.43 ± 1.84	-48.60	2.47 ± 0.35	0	0.69 ± 0.05	22.58	0.051
MVL0709	30.4	0.051	3.76	559	0	0.6	0.004	1.86	0.34	13.29 ± 1.21	-39.76	3.50 ± 0.34	0	0.74 ± 0.05	13.83	0.175*
MVL0710	18.8	0.070	12.14	517	0	0.62	0.008	2.73	3.40	18.62 ± 2.31	-48.77	17.64 ± 2.61	-65.61	1.32 ± 0.11	0	0.070
MVL0711	18.8	0.046	12.14	597	0	0.57	0.006	2.87	2.75	11.17 ± 1.75	-41.36	3.30 ± 0.55	2.88	0.79 ± 0.06	38.54	0.046
MVL0712	18.8	0.055	12.14	387	0	0.72	0.002	3.59	1.09	10.40 ± 1.46	4.27	10.21 ± 1.64	-30.43	0.72 ± 0.06	26.56	0.105*
MVL0713	20.4	0.134	9.95	324	0	0.76	0.002	1.33	0.30	23.05 ± 2.63	-10.06	24.37 ± 2.98	-60.99	1.18 ± 0.09	-24.31	0.017
MVL0717	19.5	0.115	11.11	303	0	0.78	0.002	0.99	0.30	17.04 ± 1.63	7.52	18.26 ± 3.01	-45.21	0.95 ± 0.09	-7.08	0.064
MVL0718	19.5	0.054	11.11	539	0	0.61	0.002	2.55	0.57	11.55 ± 1.45	-29.11	3.95 ± 0.74	-6.70	0.68 ± 0.05	27.11	0.054
MVL0726	18.1	0.051	13.32	417	0.16	0.7	0.002	3.21	0.96	11.09 ± 1.09	-43.63	13.17 ± 1.78	-12.49	1.08 ± 0.07	-6.67	0.009
MVL0739	22.5	0.094	7.83	938	0.05	0.33	0.002	3.45	0.51	6.38 ± 0.68	-42.56	2.00 ± 0.34	-26.50	1.00 ± 0.07	0	0.085*
MVL0740	24.1	0.130	6.62	470	0.16	0.66	0.002	1.20	0.20	15.66 ± 1.89	23.58	20.96 ± 2.17	-43.97	0.79 ± 0.06	0	0.120*
MVL0741	23.8	0.091	6.83	1386	0.37	0	0	2.82	0.00	343.28 ± 51.85	-78.08	95.43 ± 15.62	-28.53	0.94 ± 0.05	1.59	0.052
MVL0742	23.0	0.120	7.42	605	0.37	0.56	0.002	2.78	0.52	101.98 ± 13.82	0	44.33 ± 6.57	35.77	0.90 ± 0.09	0	0.096*
MVL0743	22.6	0.095	7.75	913	0.37	0.34	0.001	2.72	0.13	148.46 ± 14.14	-51.32	38.56 ± 7.52	30.07	0.90 ± 0.04	0	0.093*
MVL0744	23.4	0.108	7.12	883	0.18	0.37	0.001	1.73	0.15	13.20 ± 1.23	-34.89	2.02 ± 0.30	6.70	0.80 ± 0.05	9.73	0.108*

Table S2. Table of experimental data, inverted rheological parameters, and misfit from the three-phase rheology model. Errors of 0 fit the model within the 5 and 95% confidence interval. Boundary layer thicknesses marked with a * are larger than the channel half-width (7.5 cm), and may be expected to have significant edge effects.

Video	Temp (°C)	Height (m)	Syrup visc (Pas)	Density (kg/m ³)	Solid	Gas	Max bubble radius (m)	Max strain rate (1/s)	Capillary number	Relative consistency	Error (%)	Yield stress (Pa)	Error (%)	Flow index	Error (%)	Boundary-layer thickness (m)
MVI_0745	24.0	0.101	6.69	1063	0.26	0.24	0.000	0.90	0.02	19.84 ± ^{1.65} _{2.38}	-40.67	2.07 ± ^{0.25} _{0.44}	0	0.95 ± ^{0.07} _{0.06}	0	0.101*
MVI_0746	23.6	0.085	6.97	739	0.26	0.47	0.001	1.64	0.07	26.30 ± ^{3.99} _{2.93}	-15.46	8.30 ± ^{0.99} _{1.83}	-11.42	0.89 ± ^{0.07} _{0.06}	0	0.131*
MVI_0748	23.6	0.068	6.97	938	0.08	0.33	0.001	4.03	0.26	4.94 ± ^{0.72} _{0.53}	-20.43	2.04 ± ^{0.23} _{0.42}	-15.98	1.01 ± ^{0.04} _{0.11}	0	0.069
MVI_0749	23.7	0.058	6.90	1362	0.08	0.02	0.000	3.59	0.08	1.84 ± ^{0.34} _{0.12}	-4.94	0.50 ± ^{0.08} _{0.08}	-19.30	1.00 ± ^{0.08} _{0.05}	0	0.058
MVI_0750	22.8	0.060	7.58	1038	0.10	0.25	0.001	1.66	0.16	7.11 ± ^{1.06} _{0.69}	-47.60	7.43 ± ^{1.45} _{1.02}	-72.78	0.99 ± ^{0.07} _{0.08}	0	0.038
MVI_0751	23.5	0.064	7.04	1097	0	0.21	0.001	1.49	0.13	5.11 ± ^{0.39} _{0.64}	-56.11	2.01 ± ^{0.34} _{0.35}	-56.06	1.03 ± ^{0.06} _{0.09}	0	0.051
MVI_0752	23.5	0.080	7.04	920	0	0.34	0.002	1.50	0.20	6.43 ± ^{1.10} _{0.50}	-56.71	4.92 ± ^{0.85} _{0.77}	-64.81	0.96 ± ^{0.12} _{0.04}	0	0.060
MVI_0753	23.9	0.075	6.76	1068	0.10	0.23	0.001	1.94	0.08	7.79 ± ^{1.02} _{0.75}	-53.19	9.11 ± ^{1.44} _{1.74}	-70.81	1.11 ± ^{0.09} _{0.08}	-2.73	0.016
MVI_4775	29.1	0.073	4.18	1395	0	0	0	2.33	0.00	2.09 ± ^{0.36} _{0.18}	-43.54	0.03 ± ^{0.03} _{0.03}	708.16	0.99 ± ^{0.10} _{0.03}	0	0.073
MVI_4776	29.7	0.084	3.98	1391	0.15	0	0	5.93	0.00	3.92 ± ^{0.46} _{0.45}	-27.89	0.10 ± ^{0.02} _{0.02}	284.51	1.04 ± ^{0.04} _{0.08}	0	0.084*
MVI_4777	29.7	0.084	3.98	1391	0.15	0	0	4.37	0.00	4.19 ± ^{0.50} _{0.48}	-31.90	0.10 ± ^{0.02} _{0.02}	284.90	1.05 ± ^{0.06} _{0.07}	0	0.084*
MVI_4778	30.2	0.088	3.82	1388	0.30	0	0	4.51	0.00	10.14 ± ^{1.13} _{0.92}	-9.38	1.98 ± ^{0.34} _{0.28}	-46.07	0.94 ± ^{0.06} _{0.07}	0.02	0.096*

Table S3. Table S2 cont.

Source	Relative viscosity	Parameter values
Einstein [2]	$1 + B\phi$	$B = 1.5 - 5$
Roscoe [46]	$(1 - b\phi)^{-B}$	$b = 1 - 1.35$
Modified Einstein-Roscoe	$(1 - \frac{\phi}{\phi_m})^{-B}$	
Krieger and Dougherty [3]	$(1 - \frac{\phi}{\phi_m})^{-B\phi_m}$	$\phi_m = 0.55$
Mooney [48]	$\exp\left(\frac{B\phi}{1-\phi}\right)$	
Costa et al. [47]	$\frac{1 + \frac{\phi}{\phi_*}}{(1-F)^{B\phi_*}}, F = (1 - \xi) \operatorname{erf}\left(\frac{(\sqrt{\pi})}{2(1-\xi)} \frac{\phi}{\phi_*} \left(1 + \left(\frac{\phi}{\phi_*}\right)^\alpha\right)\right)$	$\phi_* = 0.5, \xi = 0.0005, \delta = 7, \alpha = 5$
Taylor [15]	$1 + B\phi$	$B = 1$
Llewellyn and Manga [7]	$\eta_{r \text{ inf}} + \frac{\eta_{r0} - \eta_{r \text{ inf}}}{1 + (K \cdot Ca)^m}, \eta_{r0} = (1 - \phi)^{-1}, \eta_{r \text{ inf}} = (1 - \phi)^{5/3}$	$K = 6/5, m = 2$
Princen and Kiss [11]	$32(\phi - 0.73)Ca^{-1/2}$	
Stein and Spera [14]	$1 + B\phi$	$B = 13.1$
Phan-Thien and Pham [16]	$\begin{cases} (1 - \frac{\phi_{solid}}{1 - \phi_{gas}})^{-5/2} (1 - \phi_{gas})^{-1} \\ (1 - \phi_{solid} - \phi_{gas})^{-\frac{5\phi_{solid} + 2\phi_{gas}}{2\phi_{solid} + 2\phi_{gas}}} \\ (1 - \frac{\phi_{gas}}{1 - \phi_{solid}})^{-1} (1 - \phi_{solid})^{-5/2} \end{cases}$	
Yield Stress		
Castruccio et al. [26]	$\begin{cases} 0, & \phi < \phi_c \\ D(\phi - \phi_c)^8, & \phi > \phi_c \end{cases}$	$\phi_c = 0.27, D = 5 \times 10^6$
Mueller et al. [4]	$\tau_* (1 - \phi/\phi_m)^{-2} - 1$	$\tau_* = \tau(\phi = \phi_m(1 - \sqrt{2}/2))$
Hoover et al. [49]	$A \left(\frac{\phi/\phi_c - 1}{1 - \phi/\phi_m}\right)^{1/p}$	$\phi_c = 0.25, \phi_m = 0.525, A = 5.3, p = 1$
Princen and Kiss [11]	$\frac{\sigma\phi^{1/3}}{r} (-0.080 - 0.114 \log(1 - \phi))$	
Rouyer et al. [12]	$667(\phi - 0.64)^2$	
Flow index		
Castruccio et al. [26]	$\begin{cases} 1, & \phi < \phi_c \\ C\left(\frac{\phi_c - \phi}{\phi_m}\right), & \phi > \phi_c \end{cases}$	$\phi_c = 0.27, C = 1.3$
Mueller et al. [4]	$1 - 0.2r_p(\phi/\phi_m)^4$	
Truby et al. [17]	$1 - C\phi$	$C = 0.334$

Table S4. Table of rheology models used in Fig. 3 for solid-liquid, gas-liquid, and three-phase models of relative viscosity; solid-liquid and gas-liquid models of yield stress; and solid-liquid, and three-phase models of flow index.